# CFD Analysis of Small Caliber Spinning Projectile with Variety Base Configurations

# Hassan Khormi<sup>1</sup> and Salman Alfifi<sup>2</sup>

King Fahd University of Petroleum and Minerals, Dhahran, 34464 Saudi Arabia

#### **Abstract**

Range extension got a great interest in the field of artillery and spinning projectiles. Reducing base drag is an effective way for rang extension, since it is a major component in transonic and supersonic Mach numbers. Base modification is considered as one of the implemented passive techniques to reduce base drag. This work utilizes variety of base cavities over M33 .50 cal projectile. Two size variations on projectile base are considered. This includes 2 mm and 4 mm depth. Computations are conducted using computational fluid dynamics CFD using Ansys Fluent to solve RANS equations. Simulations are performed over Mach numbers from 0.6 to 2.5. The aim of the simulations is to calculate most affecting aerodynamic forces and moments which include drag force, lift force, magnus force, magnus moment, overturning moment and spin damping moment. Then these coefficients are compared for all design variations. Results are validated by comparing with experimental and numerical results from the literature. Furthermore, a mesh independence study is done for verification. Generally, base cavity has minor effect on most of aerodynamics coefficients. Though, large base cavity has low zero-yaw drag and yaw drag relative to the reference projectile.

**Keywords:** Spinning projectile · Base drag · After-body drag · Base Cavity · Turbulent boundary layer · Drag reduction · CFD analysis.

#### List of Nomenclature and Symbols

M	Mach number	$C_D$	Drag coefficient
$\alpha_t$	Total angle of attack	$C_{D_0}$	Zero yaw drag coefficient
α	Angle of attack	$C_{D_b}$	Base drag coefficient
β	Sideslip angle	$C_{D_{\delta^2}}$	Yaw drag coefficient
V	Volume	$C_{L_{lpha}}$	Nonlinear lift coefficient
ρ	Air density	$C_{L_{\alpha_0}}$	Linear lift coefficient
v	Free stream velocity	$C_{L_{\alpha_2}}$	Cubic lift coefficient
S	Reference area	$C_{N_{p\alpha}}$	Nonlinear magnus force coefficient
p	Spin rate	$C_{N_{p\alpha_0}}$	Linear magnus force coefficient
p	Free stream pressure	$C_{N_{p\alpha_2}}$	Cubic magnus force coefficient
D	Drag force	$C_{M_{\alpha}}$	Nonlinear overturning moment coefficient
L	Lift force	$C_{M_{\alpha_0}}$	Linear overturning moment coefficient

<sup>&</sup>lt;sup>1</sup> Associate Engineer, Aerospace Engineering, g201217520@kfupm.edu.sa

<sup>&</sup>lt;sup>2</sup> Assistant Professor, Aerospace Engineering, fifis@kfupm.edu.sa

ISSN: 1004-499X Vol. 37 No. 1 (2025)

MAGF	Magnus force	$C_{M_{\alpha_2}}$	Cubic overturning moment coefficient
OM	Overturning moment or pitching moment	$C_{M_{p\alpha}}$	Nonlinear magnus moment coefficient
MAGM	Magnus moment	$C_{Mp\alpha_0}$	Linear magnus moment coefficient
SDM	Spin damping moment	$C_{M_{p\alpha_2}}$	Cubic magnus moment coefficient
T	Temperature	$C_{l_p}$	Spin Damping moment coefficient
a	Sound velocity	t	Time
$y^+$	Wall dimensionless distance	τ	Shear stress
e	Internal energy	μ	Kinematic viscosity
R	Gas constant	Q	Heat
$c_v$	Specific heat at constant volume	W	Work
k	Turbulent kinetic energy	f	Body force
ω	Specific dissipation rate	d	Projectile maximum diameter

#### 1 Introduction

Spinning projectiles, also known as Spin-Stabilized projectiles, is class of ballistics that are stabilized dynamically and gyroscopically. Ballistics is the science that deals with the motion of projectiles. Unlike ballistic missiles that are fin stabilized, spinning projectiles are not statically stable. Ballisticians began to improve accuracy of drag measurements since 1850 [1]. In 1917, M. Garnier published a table of projectile resistance function. Then, this table was modified by US army with extension to higher velocity in 1918 [2, 3]. Later, it was named as G1 drag function, referring to G1 projectile reference model. More models were then proposed reaching to G8, that include other design configurations.

For fast and low cost coefficients prediction, semi-empirical codes were developed to estimate aerodynamic coefficients and flight trajectories. Examples of these codes include Missile DATCOM [4], PRODAS [5], and Aeroprediction code [6]. However, Computational fluid dynamic CFD tools have facilitated aerodynamic simulations of complex geometry with higher accuracy than semi-empirical codes and lower cost than wind tunnel and flight experiments.

In 2002, S. Silton [7] conducted CFD simulations using Navier-Stokes solver for 12.95 mm caliber projectile, were k-ε turbulence model was applied. Then, numerical results are compared with experiments and Aeroprediction code. Results show a good agreement between Numerical and experimental approaches. In 2005, a numeri cal prediction of flight trajectory and aerodynamic characteristics was performed by J. Sahu for a finned projectile [8]. In this work, Free flight aerodynamics and trajectory are computed simultaneously using coupled CFD rigid body dynamic method, where time accurate Navier-Stokes computation is employed. Generally, good agreement was found between flight test, and computed trajectory and projectile attitude. Recently, numerical analysis was performed to calculate aerodynamic coefficients of a 120 mm projectile [9]. Coefficients of zero yaw drag, yaw drag, lift, magnus force, overturning moment and roll damping moment were predicted. SST k-ω model was selected over Spalart-Allmaras because of its better agreement with the experimental results.

Range extension got a great interest in the field of artillery and spinning projectiles. Various methods have been discussed in the literature. These methods can be classified as passive or active. Active methods include the use of controllable fins and canards, base bleed, and rocket assistance. In the contrary, passive method include optimization of boattail shape, optimization of nose and ogive, the use base cavity, and steps ahead of the base.

ISSN: 1004-499X Vol. 37 No. 1 (2025)

Attempts were made by W. Calarese in 1979 to reduce after body drag using hot gas injection and boat tailing [10]. The experiments were conducted on GAU-8 projectile at Mach 3. Different gas temperatures and boattail angles were investigated. Experimental results show total reduction in drag of 30% to 40% using slight gas injection.

Boattailing and base modification are considered as mostly used techniques to reduce base drag, which is governed by base area and base pressure [11]. In 1999, Viswanath studied various afterbody configurations for drag reduction at transonic and supersonic speeds [12]. Configurations involve multi-step, conical and circular arc boattails. Highly optimized multi-step model provides total drag reduction as much as 50%. However, the lowest drag was exhibited in the circular arc configuration.

The effect of base shape on aerodynamic coefficients was studied over Mach number from 0.7 to 2.5 [13]. steady and dynamic coefficient were computed using CFD. Investigated base shapes include square base, boattailed, chamfered base, filleted base and hemispherical base. Significant effects were found on the drag, magnus moment and pitch damping moment. The lowest exerted drag was found on boattailed and hemispherical base configurations. Though, high magnus moment was observed which leads to dynamic instability. Recently, more boattail and base design variations were studied [14]. The objective of the work is to find an optimized boattail design for base drag reduction. The baseline geometry is the M549 155 mm projectile model. Design variations include the use of riblets on the boattail and base, as well as introducing rear cavity with 15.5 mm and 23.25 mm thicknesses. However, the lowest drag was found at the 15.5 mm thickness cavity.

The purpose of the present work is to utilize the base cavity technique over an existing projectile. Computations will be carried out using computational fluid dynamics CFD using Ansys Fluent to solve RANS equations. The aim of design modifications is to minimize projectile drag. Thus, results of drag and other steady aerodynamic coefficients will be compared. Aerodynamic coefficients will be determined, which include drag force, lift force, magnus force, magnus moment, spin damping moment and overturning moment. Then these coefficients will be compared for each design variation.

# 2 Methodology

# 2.1 Aerodynamic forces and moments

NACA and BRL aeroballistics are common system in defining aerodynamic coefficients. BRL aeroballistics system is adopted throughout this work [15]. Yawing motion in aeroballistics describes any combined pitching and yawing motions. In addition, yaw angle is known as total angle of attack [16]. The definition of total angle of attack is given by [1, 16]

$$\sin \alpha_t = \sqrt{(\sin \alpha \cos \beta)^2 + \sin^2 \beta} \tag{1}$$

For  $(\alpha_t < 15 \text{ degrees})$ , a good approximation for total angle of attack is

$$\alpha_t \approx \sqrt{\alpha^2 + \beta^2} \tag{2}$$

## - Drag force

Direction of drag force opposes projectile forward velocity. It consists of skin friction, wave drag and base drag. Drag force is given by

$$D = \frac{1}{2} \rho v^2 S C_D \tag{3}$$

The reference area S is defined by:

$$S = \frac{\pi d^2}{4} \tag{4}$$

Where d is the reference diameter which is taken as the diameter of the cylindrical section.

 $C_D$  is the total drag coefficient which composes of zero-yaw drag coefficient and yaw drag coefficient. Both components vary with Mach number.

ISSN: 1004-499X Vol. 37 No. 1 (2025)

$$C_D = C_{D_0} + C_{D_{s2}} \delta^2 \tag{5}$$

$$\delta = \sin \alpha_t \tag{6}$$

#### Lift force

Lift force is the force perpendicular to the trajectory, and it can be calculated as

$$L = \frac{1}{2}\rho v^2 S C_{L_{\alpha}} \sin \alpha_t \tag{7}$$

$$C_{L_{\alpha}} = C_{L_{\alpha_0}} + C_{L_{\alpha_2}} \delta^2 \tag{8}$$

#### - Magnus force

As projectile spins with small angle of attack, a weak asymmetry of the boundary layer is induced which causes unequal pressure around projectile body. Hence, magnus force is produced [17, 18]. Its direction depends on the directions of angle of attack and spin. However, it is given by

$$MAGF = \frac{1}{2}\rho v^2 S\left(\frac{pd}{V}\right) C_{N_{p\alpha}} \sin \alpha_t \tag{9}$$

$$C_{N_{p\alpha}} = C_{N_{p\alpha_0}} + C_{N_{p\alpha_2}} \delta^2 \tag{10}$$

## - Overturning moment

Overturning moment is associated with lift force and it is also known as pitching moment. It is given by [1, 19, 16]

$$OM = \frac{1}{2}\rho v^2 SdC_{M_{\alpha}} \sin \alpha_t \tag{11}$$

$$C_{M_{\alpha}} = C_{M_{\alpha_0}} + C_{M_{\alpha_2}} \delta^2 \tag{12}$$

#### - Magnus moment

Magnus moment depends on the distribution of magnus force, flight Mach number and yaw angle. Usually, the acting magnus force can be neglected. However, magnus moment should be considered, because high magnus moment can cause dynamic instability [1, 13]. Magnus moment is given by

$$MAGM = \frac{1}{2}\rho v^2 Sd\left(\frac{pd}{V}\right) C_{M_{p\alpha}} \sin \alpha_t \tag{13}$$

$$C_{M_{p\alpha}} = C_{M_{p\alpha_0}} + C_{M_{p\alpha_2}} \delta^2 \tag{14}$$

It is important to mention that the center of pressure of lift force is different from the center of pressure of magnus force.

# - Spin damping moment

Spin damping moment is the moment that acts to reduce the spinning and its direction always opposes projectile spinning direction. As a standard a factor of  $\left(\frac{pd}{V}\right)$  is maintained to calculate damping coefficient and to account for difference in velocity. Thus, it is calculated by

$$SDM = \frac{1}{2}\rho v^2 Sd\left(\frac{pd}{V}\right) C_{l_p} \tag{15}$$

# 2.2 Governing equations

Basically, conservation of mass and momentum is implemented. Because of flow high speed, compressibility was accounted. Hence, energy equation and ideal gas equation were solved. In addition, Sutherland's law is included to account for the effect of heat on air viscosity, which enhances model credibility.

ISSN: 1004-499X Vol. 37 No. 1 (2025)

#### 1. Conservation of mass (Continuity equation).

The conservation form of the continuity equation, which is derived on the basis of a fixed finite control volume in space, can be written in differential form as

$$\frac{\partial \rho}{\partial t} + \nabla \cdot (\rho V) = 0 \tag{16}$$

It tells that the net mass flow out of control volume through surface S equals the time rate of decrease of mass inside the control volume V.

## 2. Conservation of momentum (Navier-Stokes equations).

Momentum equations can be represented in differential form and are known as Navier-Stokes equations. For three-dimensional flow it can be written in conservative form in x, y, and z as

$$\frac{\partial(\rho u)}{\partial t} + \frac{\partial(\rho u^2)}{\partial x} + \frac{\partial(\rho uv)}{\partial y} + \frac{\partial(\rho uw)}{\partial z} \\
= -\frac{\partial p}{\partial x} + \frac{\partial}{\partial x} \left(\lambda \nabla \cdot V + 2\mu \frac{\partial u}{\partial x}\right) + \frac{\partial}{\partial y} \left[\mu \left(\frac{\partial v}{\partial x} + \frac{\partial u}{\partial y}\right)\right] + \frac{\partial}{\partial z} \left[\mu \left(\frac{\partial u}{\partial z} + \frac{\partial w}{\partial x}\right)\right] + \rho f_x \tag{17}$$

$$\frac{\partial(\rho v)}{\partial t} + \frac{\partial(\rho u v)}{\partial x} + \frac{\partial(\rho v^2)}{\partial y} + \frac{\partial(\rho v w)}{\partial z} \\
= -\frac{\partial p}{\partial y} + \frac{\partial}{\partial x} \left[ \mu \left( \frac{\partial v}{\partial x} + \frac{\partial u}{\partial y} \right) \right] + \frac{\partial}{\partial y} \left( \lambda \nabla \cdot V + 2\mu \frac{\partial v}{\partial y} \right) + \frac{\partial}{\partial z} \left[ \mu \left( \frac{\partial w}{\partial y} + \frac{\partial v}{\partial z} \right) \right] + \rho f_y \tag{18}$$

$$\frac{\partial(\rho w)}{\partial t} + \frac{\partial(\rho uw)}{\partial x} + \frac{\partial(\rho vw)}{\partial y} + \frac{\partial(\rho w^2)}{\partial z} \\
= -\frac{\partial p}{\partial z} + \frac{\partial}{\partial x} \left[ \mu \left( \frac{\partial u}{\partial z} + \frac{\partial w}{\partial x} \right) \right] + \frac{\partial}{\partial y} \left[ \mu \left( \frac{\partial w}{\partial y} + \frac{\partial v}{\partial z} \right) \right] + \frac{\partial}{\partial z} \left( \lambda \nabla \cdot V + 2\mu \frac{\partial w}{\partial z} \right) + \rho f_z \tag{19}$$

The above three equations represent the complete form of Navier-Stokes equations, in which unsteady, viscous, compressible and three-dimensional flow is described. Appeared forces on fluid element composes of pressure force, viscous force, including shear and normal stresses, and body forces such as gravity and electromagnetic forces.

## 3. Conservation of energy (Energy equation).

Energy equation states that rate of change of energy inside fluid element equal to the net heat flux into element plus the rate of work done on element due to body and surface forces. Essentially, it is derived from the first law of thermodynamic, which states that the change of internal energy of fluid element equals the change of heat added and work done on that fluid element, or mathematically: dq + dw = de

The complete energy equation can be written on differential form as

$$\frac{\partial(\rho e)}{\partial t} + \nabla \cdot (\rho eV)$$

$$= \rho + \frac{\partial}{\partial x} \left( k \frac{\partial T}{\partial x} \right) + \frac{\partial}{\partial y} \left( k \frac{\partial T}{\partial y} \right) + \frac{\partial}{\partial z} \left( k \frac{\partial T}{\partial z} \right) - p \left( \frac{\partial u}{\partial x} + \frac{\partial v}{\partial y} + \frac{\partial w}{\partial z} \right) + \lambda \left( \frac{\partial u}{\partial x} + \frac{\partial v}{\partial y} + \frac{\partial w}{\partial z} \right)^{2} + \mu \left[ 2 \left( \frac{\partial u}{\partial x} \right)^{2} + 2 \left( \frac{\partial v}{\partial y} \right)^{2} + 2 \left( \frac{\partial u}{\partial z} \right)^{2} + \left( \frac{\partial u}{\partial y} + \frac{\partial v}{\partial z} \right)^{2} + \left( \frac{\partial u}{\partial z} + \frac{\partial w}{\partial z} \right)^{2} \left( \frac{\partial v}{\partial z} + \frac{\partial w}{\partial y} \right)^{2} \right] \tag{20}$$

## 4. Perfect gas equation.

Since the simulated flow is compressible, which means that the density varies spatially and timely, perfect gas equation is utilized to calculate the change in flow density throughout the domain. It relates density to flow pressure and temperature by

$$p = \rho RT \tag{21}$$

In Ansys fluent, different form of perfect gas equation is used which is written as

ISSN: 1004-499X Vol. 37 No. 1 (2025)

$$\rho = \frac{p_{op} + p}{\frac{R}{M_w}T} \tag{22}$$

Where  $p_{op}$  is the operating pressure and  $M_w$  is molecular weight.

#### 5. Equation of estate

Above are four equations, though they involve five unknown variables. Thay are V, T,  $\rho$ , e, and p. Therefore, additional equation is required to complete the system, in which it will be a thermodynamic state relation for e that is applicable for calorically perfect gas.

$$e = c_{v}T \tag{23}$$

#### 6. Sutherland law.

To enhance the credibility of the simulation, the variation of air viscosity with temperature is considered by the Sutherland law. It is given by

$$\frac{\mu}{\mu_0} = \left(\frac{T}{T_0}\right)^{3/2} \frac{T_0 + 110}{T + 110} \tag{24}$$

Here,  $\mu_0$  and  $T_0$  are viscosity and temperature at a selected reference condition, respectively. In this work the reference condition is the standard sea level.

# 2.3 Configurations and meshing

M33 is the selected projectile for this study. It is a .50cal projectile. Geometry, mass properties and aerodynamic characteristics was obtained from [1, 7, 20]. Base modifications will be studied in the following sequence:

- Aerodynamic analysis will be conducted over the original design of M33 and results will be validated with the experimental values. Detailed dimension of the projectile is shown in Figure 1. This configuration is denoted later by M33.
- 2. Cavity of 2 mm depth is introduced on projectile base, which is presented in Figure 2. This creates a sort of vacuum at the base to decrease the effect of adverse pressure gradient. This configuration is denoted later by SBC which stands for small base cavity.
- 3. A larger cavity of depth 4 mm is introduced, as in Figure 3. Results of this configuration will be compared to the preceding configuration to investigate the effect of cavity size. This configuration is denoted later by LBC which stands for large base cavity.

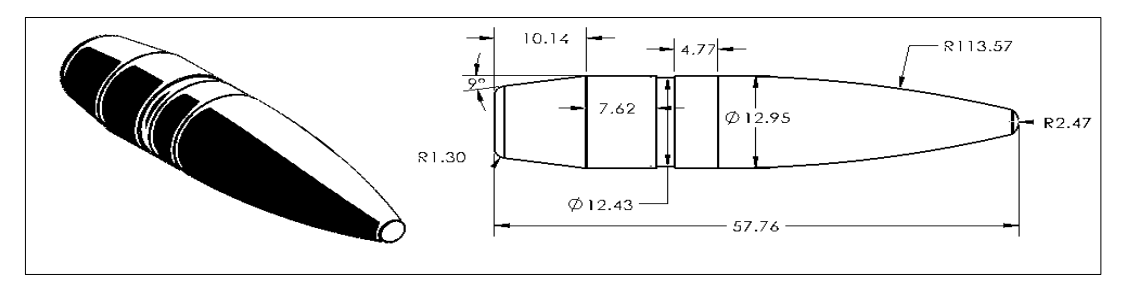


Figure 1. Original M33 Geometry (mm).

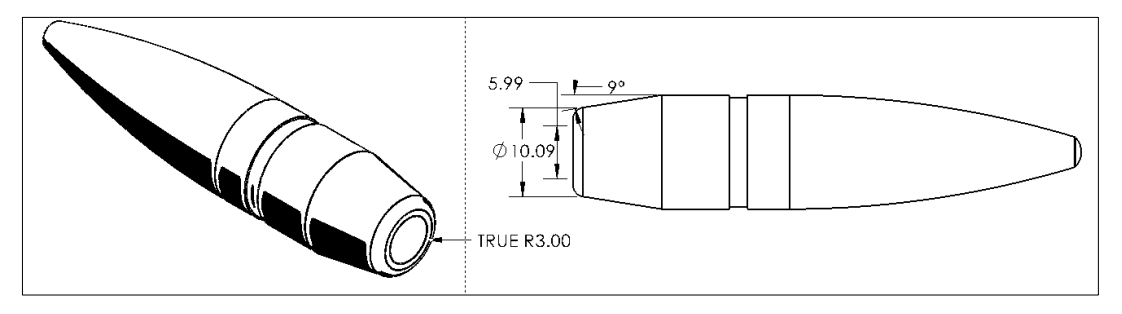


Figure 2. 2 mm depth base cavity (mm).

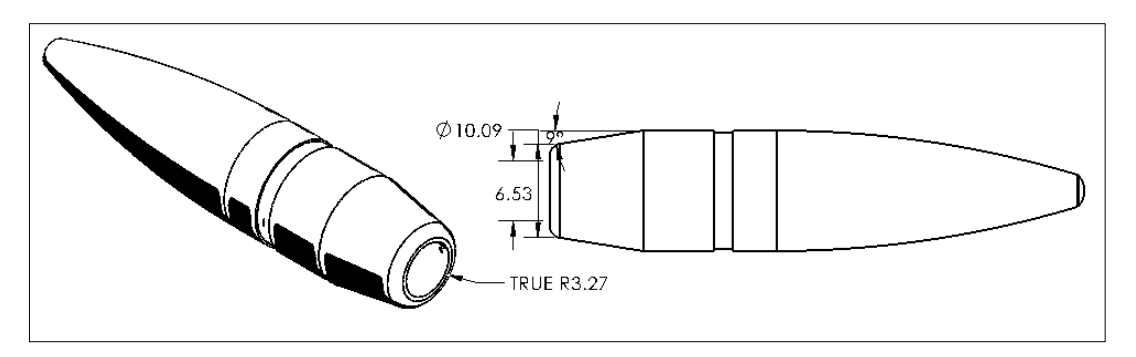


Figure 3. 4 mm depth base cavity (mm).

Meshing domain is selected to be spherical with radius that is ten times projectile length, as shown in Figure 4. Then a cylindrical subdomain of influence is applied near the projectile to increase mesh elements in that region which appears in Figure 5. The radius of the subdomain is two times caliber size while the length is three times projectile length. Furthermore, inflation layers, of 1.2 growth rate, were generated on the surface that covers boundary layer region and satisfy the requirement of the dimensional wall displacement parameter (y+) which is shown in Figure 6. The mesh is created using local sizing on surfaces with a growth rate of 1.15, As can be seen in Figures 7 through 9, where grids consist of tetrahedral elements with prism layers.

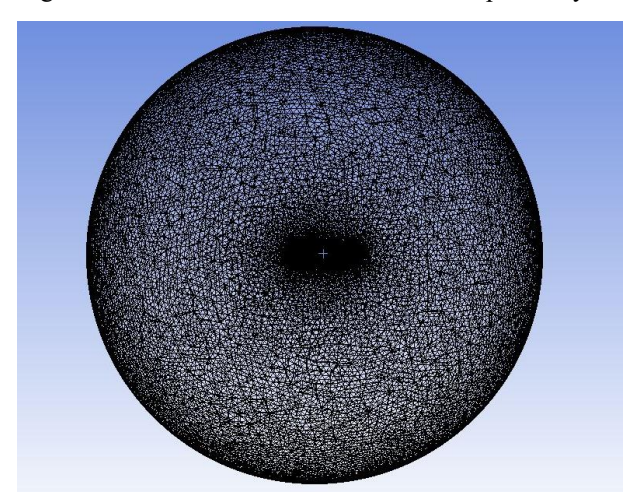


Figure 4. Outer domain mesh [21].

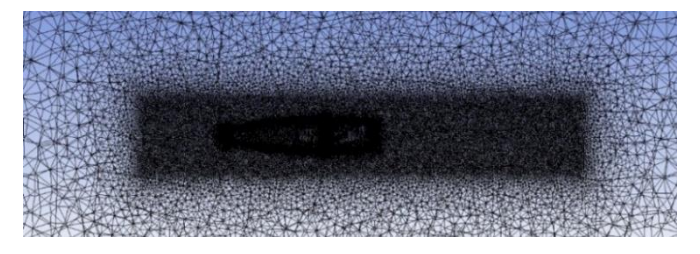


Figure 5. Domain of influence [21].

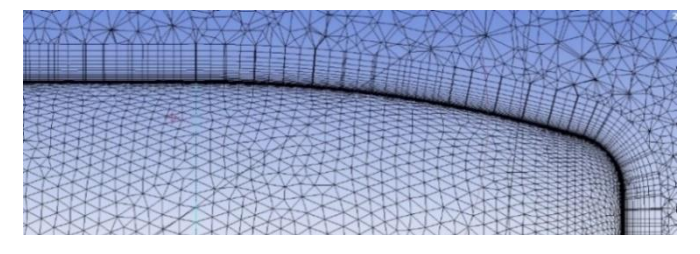


Figure 6. Mesh inflation prism layers [21].

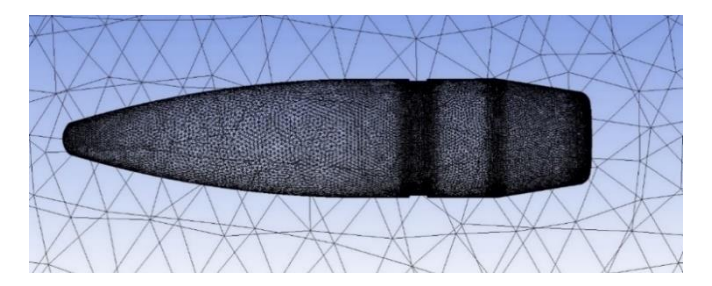


Figure 7. Original configuration surface mesh [21].

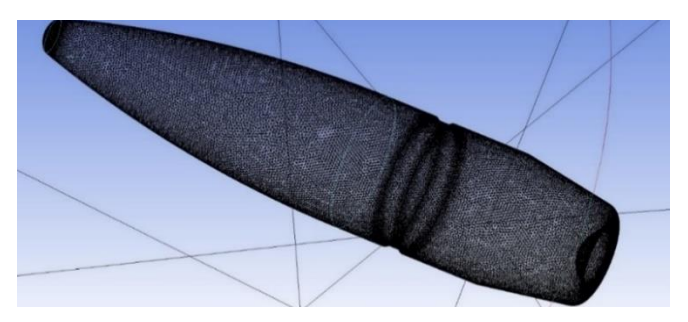


Figure 8. 2mm base cavity surface mesh [21].

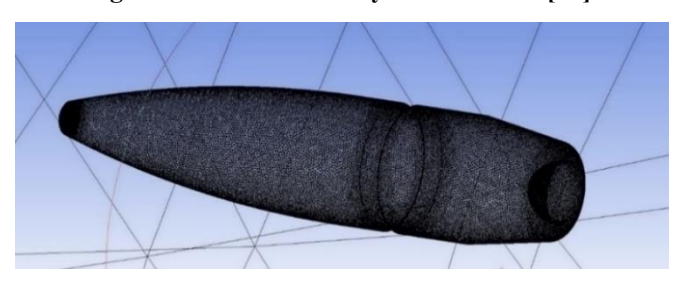


Figure 9. 4mm base cavity surface mesh [21].

# 2.4 Pre-processing setups

At first, RANS calculations over the different projectile configurations are carried out with freestream Mach numbers that enclose most of flight regimes. Namely at 0.6, 0.8, 0.9, 1.0, 1.1, 1.2, 1.5, 2.0, and 2.5 Mach numbers. Also, these speeds encompass most of spinning projectiles flying envelopes. In order to calculate coefficients derivatives such as  $C_{L_{\alpha_0}}$  and  $C_{M_{\alpha_0}}$ , the simulations were conducted over zero, 2, and 4 degrees angles of attack.

Shear stress transport SST  $k-\omega$  is the main turbulence model used for the different design configurations. According to literature, SST  $k-\omega$  model performs well in capturing and modelling flow separation. Therefore, it was chosen for the analysis and simulation of base drag.  $k-\omega$  model is categorized under Boussinesq family, in which Reynold stresses are related to mean velocity gradients. The transport equations of SST  $k-\omega$  are similar to the standard  $k-\omega$  model transport equations. Nevertheless, in SST the model changes gradually from standard  $k-\omega$  at the inner region of boundary layer or what is known as viscous sublayer, to  $k-\varepsilon$  in the outer region of boundary layer. That is done according to the performance of both models in the designated regions.

During the computations air properties are set to sea level condition. Projectile spin rate defers at each free stream velocity so that the nondimensional rotating velocity parameter equals 0.2135 [7], defined by the relation

$$\frac{pd}{t^2} = 0.2135$$

Here, p is the spin rate in rad/s, d is the projectile caliber in m, and v is the freestream velocity in m/s. Table 1 illustrates spin rate that corresponds to each simulated Mach number.

Table 1. Spin rate corresponding to each Mach number.

Mach number	Spin rate (rad/s)
0.6	3367
0.8	4489
0.9	5050
1	5611
1.1	6173
1.2	6733
1.5	8417
2	11223
2.5	14028

ANSYS Fluent of version 2022 R1 was used for all CFD calculations. During RANS calculations, the solver was set to density based solver, since flow speed varies from subsonic to high supersonic and compressible flow is assumed. Solution Scheme is selected to be implicit and gradient terms were computed using least square cell-based method. The governing equations are discretized by the second-order upwind scheme. In the outer domain, the boundary condition is set to pressure far-field with sea level pressure and temperature. For the bullet surface, a no slip condition is set with rotating wall to simulate projectile spinning and to allow for the calculation of magnus force, magnus moment and spin damping moment. Here, the resulted forces and moments are nondimensionalized by the parameters appearing in Table 2.

Table 2. Nondimensionalizing parameter of aerodynamic forces and moments.

Force and moment coefficient	Nondimensionalizing parameter
Drag force Coefficient $(C_D)$	$\frac{1}{2} \rho v^2 S$
Lift force Coefficient $(C_L)$	$\frac{1}{2} \rho v^2 S$
Magnus force Coefficient $(C_{Np})$	$\frac{1}{2} \rho v^2 S \frac{pd}{v}$
Magnus moment Coefficient ( $C_{mp}$ )	$\frac{1}{2} \rho v^2 S d \frac{pd}{v}$
Overturning moment Coefficient $(C_m)$	$\frac{1}{2} \rho v^2 S d$
Spin damping moment Coefficient $(C_{lp})$	$\frac{1}{2} \rho v^2 S d \frac{pd}{v}$

#### 3 Mesh independence study and y+

The aim of mesh independence study is to avoid any numerical error caused by mesh resolution. Also, the y+ value will be assessed at each mesh. Initially a 1.3 million mesh element was created, and the value of drag coefficient and y+ is evaluated. A 0.005 mm thickness of the inflation's first layer resulted in 1.9 y+ value. Thus, mesh resolution is improved and first layer thickness is decreased which leads to improvement in y+ value. Also drag coefficient becomes constant as mesh resolution increases. Table 3 presents mesh element count and first

layer thickness corresponding to drag coefficient and y+. The simulations in the table were conducted over M33 original configuration at 1.5 Mach number and zero angle of attack.

Mesh Element count (million)	Inflation first layer thickness (mm)	CD	<b>y</b> +
1.3	0.005	0.384	1.9
2.4	0.005	0.379	1.9
4.6	0.005	0.367	1.9
5.4	0.003	0.363	1.2
6.1	0.002	0.363	0.8
6.9	0.002	0.363	0.8
8.7	0.002	0.363	0.8

Table 3. Mesh independence over M33 at M = 1.5.

From the above table, the selected mesh is the 6.1 million elements with 0.002 thickness of the inflation's first layer. It can be noticed that drag coefficient is not changing with mesh resolution and y+ reached a value less than 1.0. Subsequently, the total number of inflation layers needed is 25 layers with a growth rate of 1.2. Therefore, similar meshing method are applied to the subsequent configurations. Figure 10 Shows y+ on bullet surface at the maximum speed that is M=2.5. Most of the surfaces have a y+ value around 0.6. Although, at the nose it reaches a value of 2.62, and the area weighted average does not exceed 0.8.

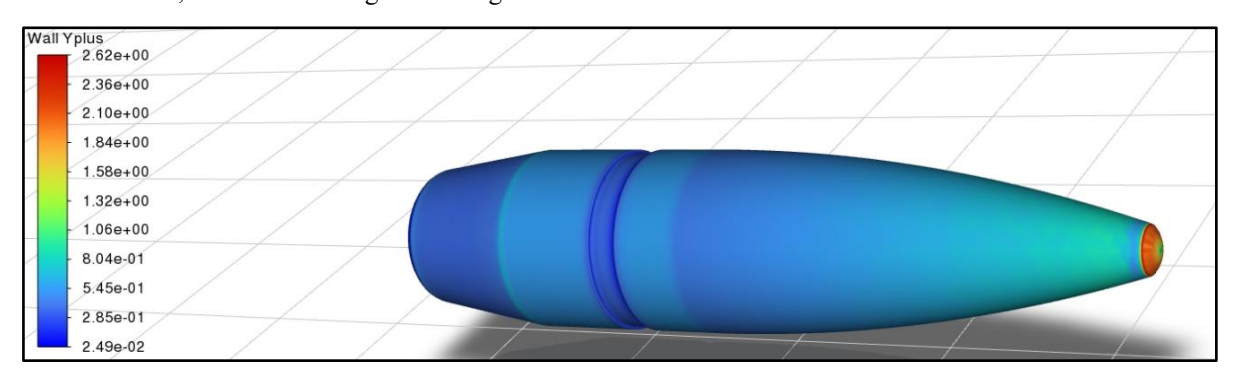


Figure 10. Wall y+ over M33 at 2.5 Mach number [21].

#### 4 Results Validation

McCoy conducted a wind tunnel test ranging from 0.75 to 2.66 Mach number [22]. Also, S. Silton studied the projectile numerically from 0.7 to 2.7 Mach numbers, where the mesh consists of 5.4 million cells [7]. The results of both researches are compared to this work for validation and they are depicted in Figure 11. It can be seen that CFD overpredict zero-yaw drag, especially in transonic and supersonic Mach numbers. Furthermore, the current study predicts the value of drag coefficient better than the results from [7].

Another paper by S. Silton and S. Dinavahi investigated the M33 [11]. It concerned about the base drag. It discovered a phenomenon of negative base drag in the subsonic flow. Firstly, it was proved that this phenomenon is not numerical. Additionally, it was interpreted by the base curvature which accelerates the flow and leads to an increase in the base pressure. Thus, this work has investigated this phenomenon and compared the result with Silton and Dinavahi work. Figure 12 validates base drag at the subsonic flow regimes, and good agreement can be inferred between the two works.

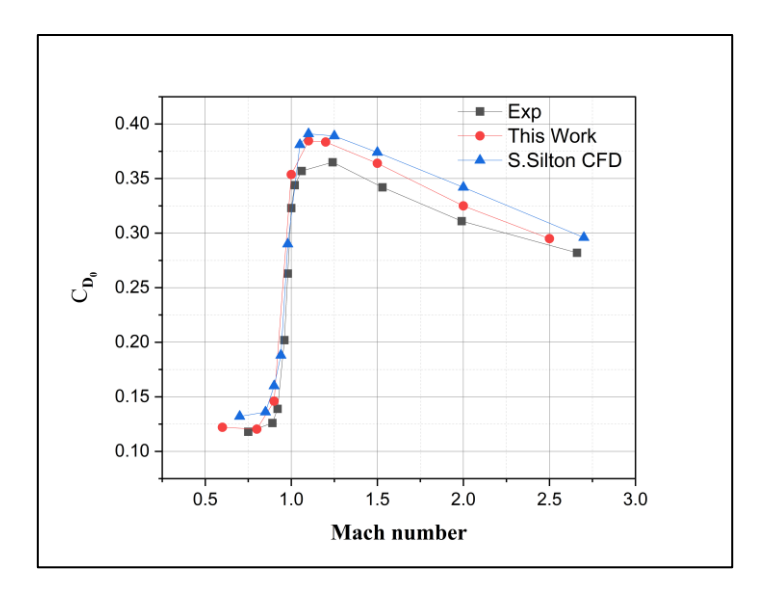


Figure 11. Zero-yaw drag comparison with experimental and numerical results.

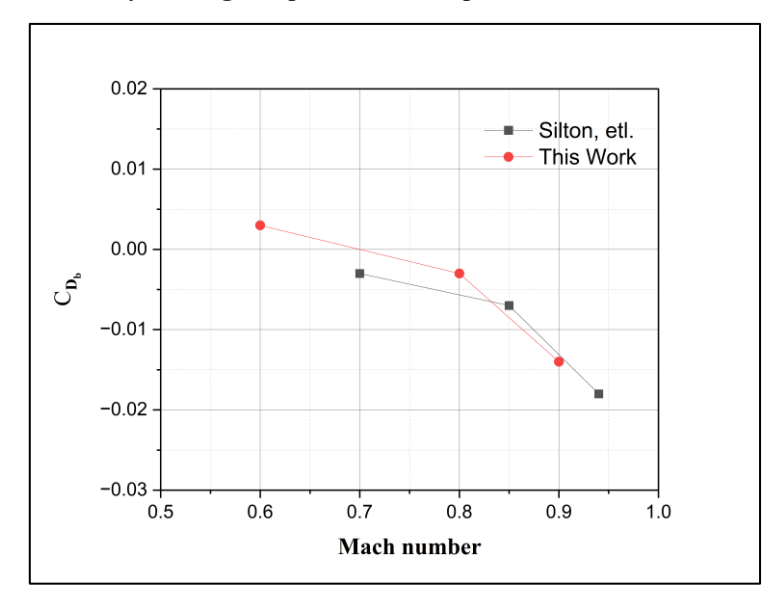


Figure 12. Base drag comparison with numerical results in subsonic flow.

## 5 Results

First, differences in drag coefficient are investigated, which is the most affecting factor on projectile range. Next, the remaining coefficients are examined and effect of design features are highlighted. Figure 13 shows a comparison of the zero yaw drag coefficient from 0.6 to 2.5 Mach number. It can be noticed that base cavity performs well in high supersonic flow regimes, while it has an adverse effect in the transonic speeds. Examining the drag at Mach numbers 0.6, 0.8 and 0.9, it can be inferred that the larger the base cavity size the higher is the zero-yaw drag. Generally, the SBC configuration provides either larger values in drag or similar to the original configuration. However, the LBC configuration provides lower drag than the M33 above 1.5 Mach numbers.

The comparison of base drag coefficient appears in Figure 14. Examining the SBC, it encounters high base drag, especially at 1.2 and 2.0 Mach numbers. In the subsonic speeds, the effect of base cavity on base drag is minimal and unnoticeable. In addition, LBC has relatively low base drag in the supersonic regime.

In Table 4, drag coefficients are shown. Also, it represents the ratio of base drag to zero yaw drag to give more insights about them. The negative sign indicates a negative base drag. Overall, LBC is the lower in base to zero yaw drag ratio. However, it can be inferred that the ratio reaches its maximum at 1.5 and 2.0 Mach numbers.

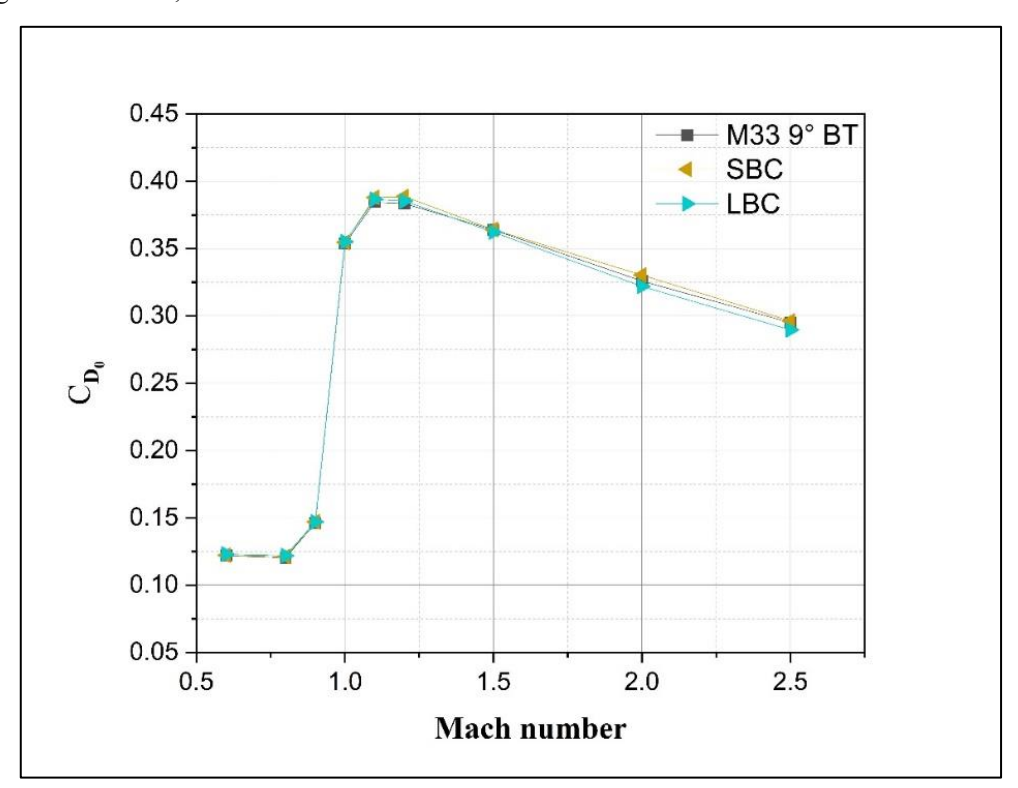


Figure 13. Zero yaw drag coefficient versus Mach number for different configurations.

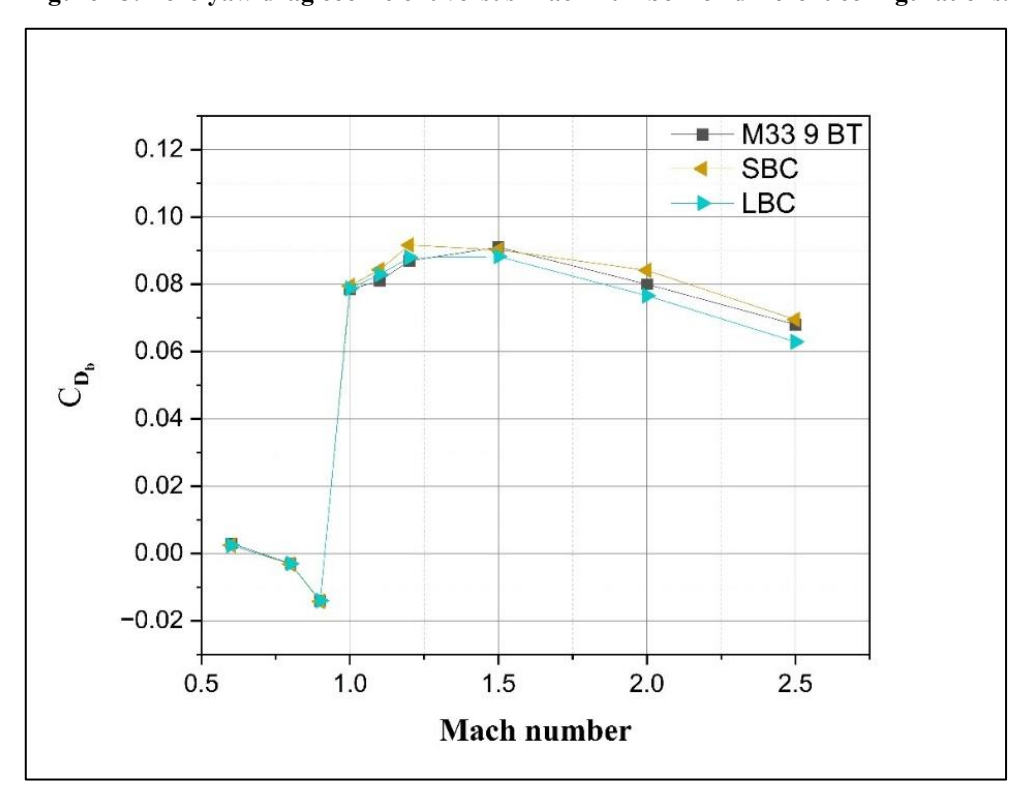


Figure 14. Base drag coefficient versus Mach number for different configurations.

Coefficient	Configuration	0.6	0.8	0.9	1	1.1	1.2	1.5	2	2.5
-	M33	0.122	0.120	0.146	0.354	0.385	0.384	0.364	0.326	0.295
$C_{D_0}$	SBC	0.122	0.121	0.147	0.355	0.388	0.389	0.364	0.330	0.296
	LBC	0.123	0.122	0.147	0.355	0.387	0.385	0.362	0.322	0.290
$C_{D_b}$	M33	0.003	-0.003	-0.014	0.079	0.081	0.087	0.091	0.080	0.068
	SBC	0.002	-0.003	-0.014	0.080	0.084	0.092	0.090	0.084	0.070
	LBC	0.002	-0.003	-0.014	0.079	0.083	0.088	0.088	0.077	0.063
$C_{D_b}/C_{D_0}$ (%)	M33	2.46%	-2.49%	-9.59%	22.19%	21.06%	22.69%	25.00%	24.54%	23.05%
	SBC	2.01%	-2.61%	-9.70%	22.42%	21.73%	23.57%	24.78%	25.46%	23.45%
	LBC	1.95%	-2.46%	-9.53%	22.17%	21.44%	22.82%	24.36%	23.79%	21.72%

Looking at the linear lift coefficient in Figure 15, both SBC and LBC configurations show lower lift slope from subsonic to supersonic speed than M33. This gives advantage at long ranges where yaw of repose affects projectile trajectory. However, at Mach 2.0 the difference in lift slope between LBC and M33 become inconsiderable, while SBC approaches M33 values at Mach 2.5.

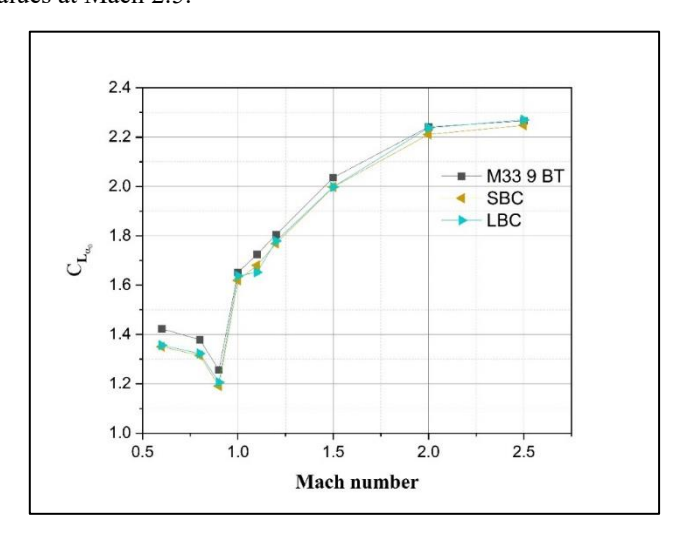


Figure 15. Linear lift coefficient versus Mach number for different configurations.

Figure 16 represents the linear overturning moment coefficient. It should be noted that at all condition the value of the moment coefficient slope is positive and this is reasonable, since spinning projectile are not statically stable. However, the degree of static stability differs among the configurations. Overall, LBC and SBC shows slightly higher linear overturning moment coefficient than M33 over the different speed ranges.

The linear magnus force and magnus moment coefficients are presented in Figure 17 and Figure 18, respectively. It is important to highlight that in magnus moment prediction, large errors were noticed at subsonic and transonic speeds, with counter estimation in moment direction. This refers to lack of prediction of magnus force center of

pressure, when utilizing RANS models. However, at 2.5 Mach number a good estimation was provided with around 2% difference. This was also concluded by [23] in which it addresses the need for detached eddy simulation model in estimating magnus moment for M < 2.0.

A plot of spin damping moment versus Mach number is presented by Figure 19. The negative sign indicates the direction. As can be seen for all configuration, the spin damping moment coefficient decreases as Mach number increases. Though, there are some discrepancies around Mach 1.0. For supersonic regime and as speed increases, the differences in spin damping moment become noticeable. Additionally, a very slight decrease in spin damping is noticed with angle of attack because of partial flow separation that leads to decrease in shear stress.

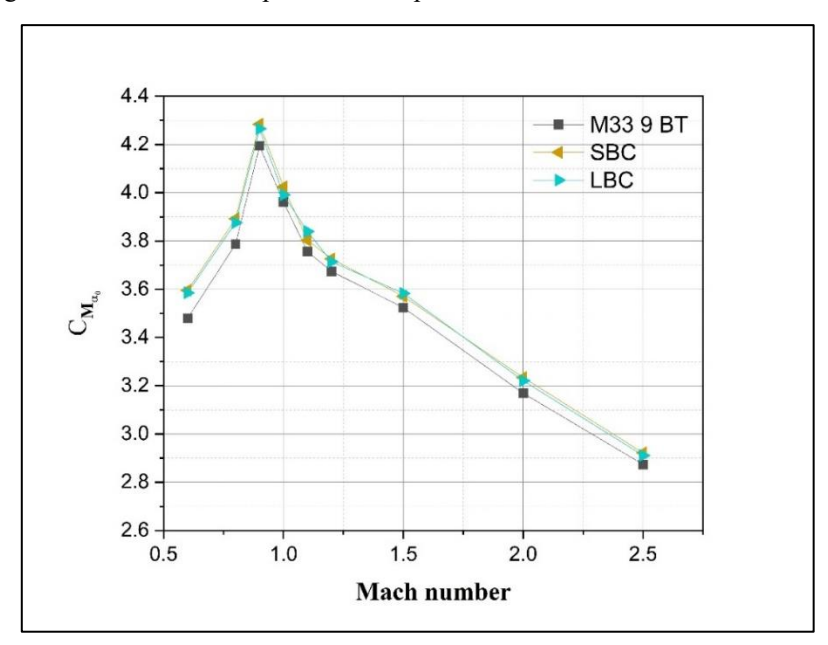


Figure 16. Linear overturning moment coefficient versus Mach number for different configurations.

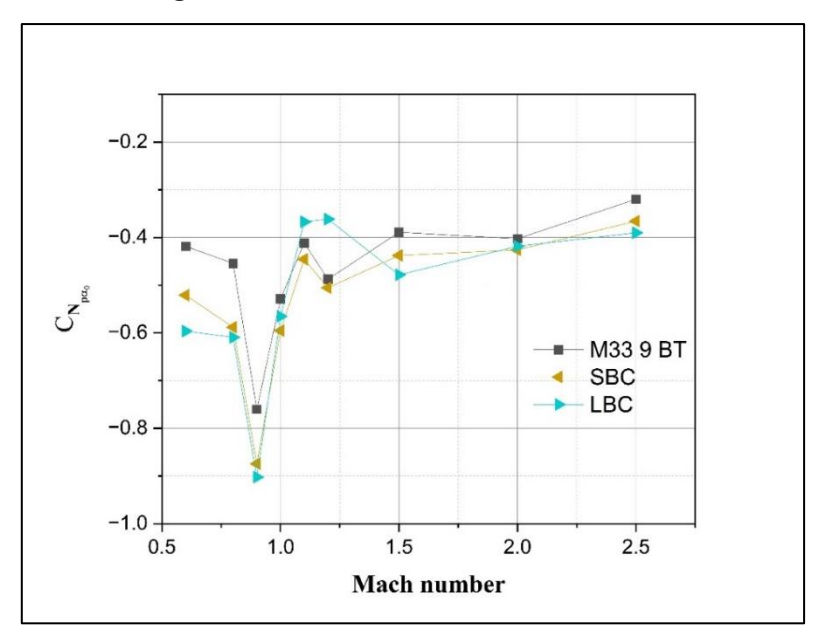


Figure 17. Linear magnus force coefficient versus Mach number for different configurations.

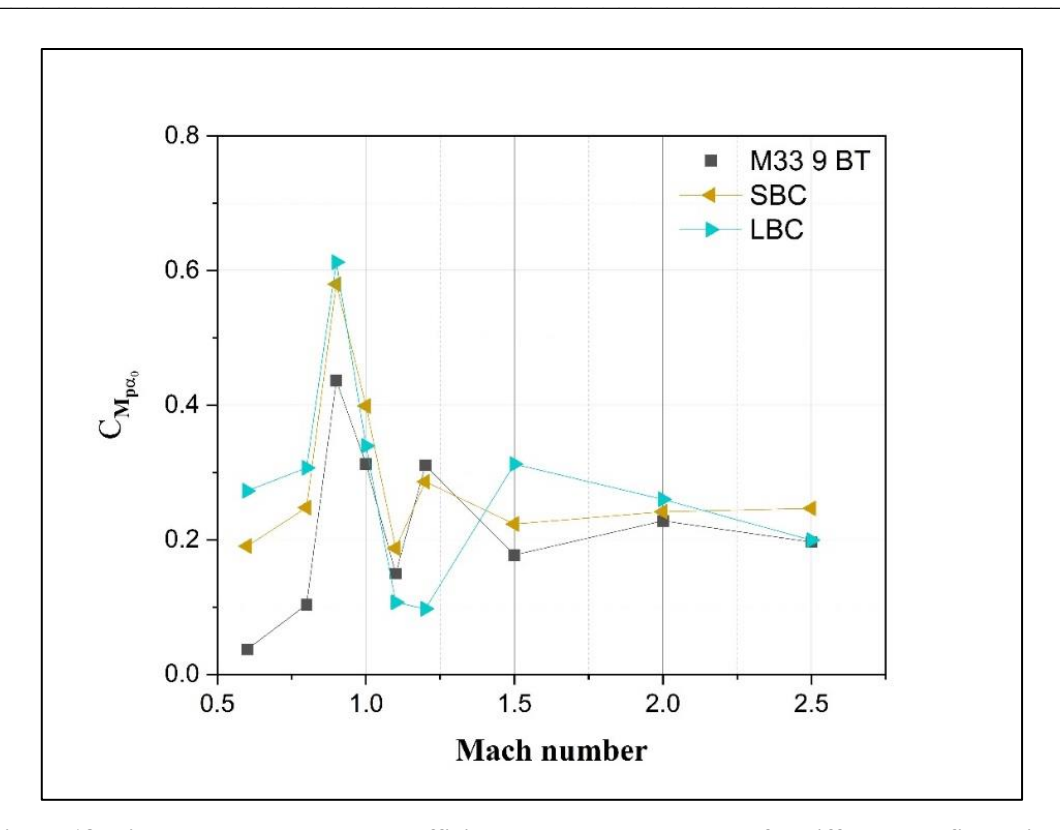


Figure 18. Linear magnus moment coefficient versus Mach number for different configurations.

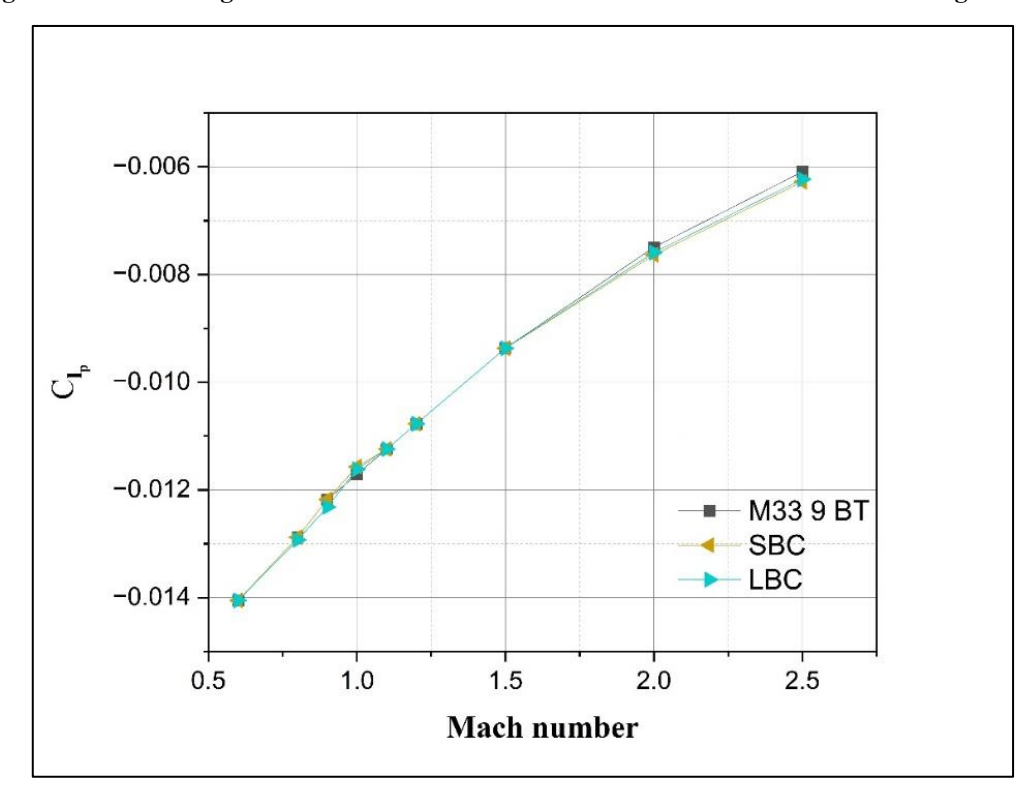


Figure 19. Spin damping moment coefficient versus Mach number for different configurations.

Results of the nonlinear aerodynamic coefficients are presented in Table 5 explicitly, which are not depicted in the charts above. Yaw drag shows a considerable reduction with larger base cavity.

Table 5. Tabulated non-linear aerodynamic coefficients.

				$C_{D_{\delta^2}}$					
Mach Number	0.6	0.8	0.9	1	1.1	1.2	1.5	2	2.5
M33	3.12	3.32	3.04	5.74	6.16	4.31	6.24	6.65	7.797
SBC	3.985	3.98	3.139	5.597	6.036	4.493	4.645	6.086	5.097
LBC	4.703	4.317	3.213	5.967	6.233	4.259	10.73	5.499	3.426
				$C_{L_{\alpha_2}}$					
Mach Number	0.6	0.8	0.9	1	1.1	1.2	1.5	2	2.5
M33	-39.19	-17.24	15.67	17.24	7.84	-0.001	3.13	29.78	28.21
SBC	-1.019	15.36	42.85	27.04	15.83	9.796	15.75	28.92	35.89
LBC	18.81	27.12	46.71	21.63	29.31	10.66	13.32	33.23	38.87
				$C_{N_{p\alpha_2}}$					
Mach Number	0.6	0.8	0.9	1	1.1	1.2	1.5	2	2.5
M33	-25.7	-12.55	7.34	12.85	-14.68	14.68	-22.02	0.00	-18.36
SBC	25.70	47.73	18.36	13.95	7.78	7.34	-13.58	5.58	-5.51
LBC	29.66	26.43	35.97	8.07	-21.88	-42.95	5.73	6.97	20.56
				$C_{M_{\alpha_2}}$					
Mach Number	0.6	0.8	0.9	1	1.1	1.2	1.5	2	2.5
M33	39.97	18.81	-14.11	-25.86	-14.11	-2.353	-0.0017	29.0	15.67
SBC	-14.89	-28.37	-49.61	-42.32	-16.46	-10.97	-12.23	-19.2	-23.9
LBC	-39.03	-41.93	-53.29	-34.41	-32.13	-12.54	-15.68	-26.65	-22.26
				$C_{M_{p\alpha_2}}$					
Mach Number	0.6	0.8	0.9	1	1.1	1.2	1.5	2	2.5
M33	30.10	16.15	-9.91	-22.02	3.67	-40.38	13.95	0.00	14.68
SBC	-46.25	-33.51	-24.23	-23.49	-22.76	-14.68	14.17	0.37	-14.76
LBC	-36.71	-33.41	-40.74	-13.07	17.69	38.91	-28.78	-11.38	8.07

Maximum pressure coefficients at the base are tabulated in Table 6. They are arranged by the colors, where green colors indicate positive values. Darker colors mean high value in pressure coefficient.

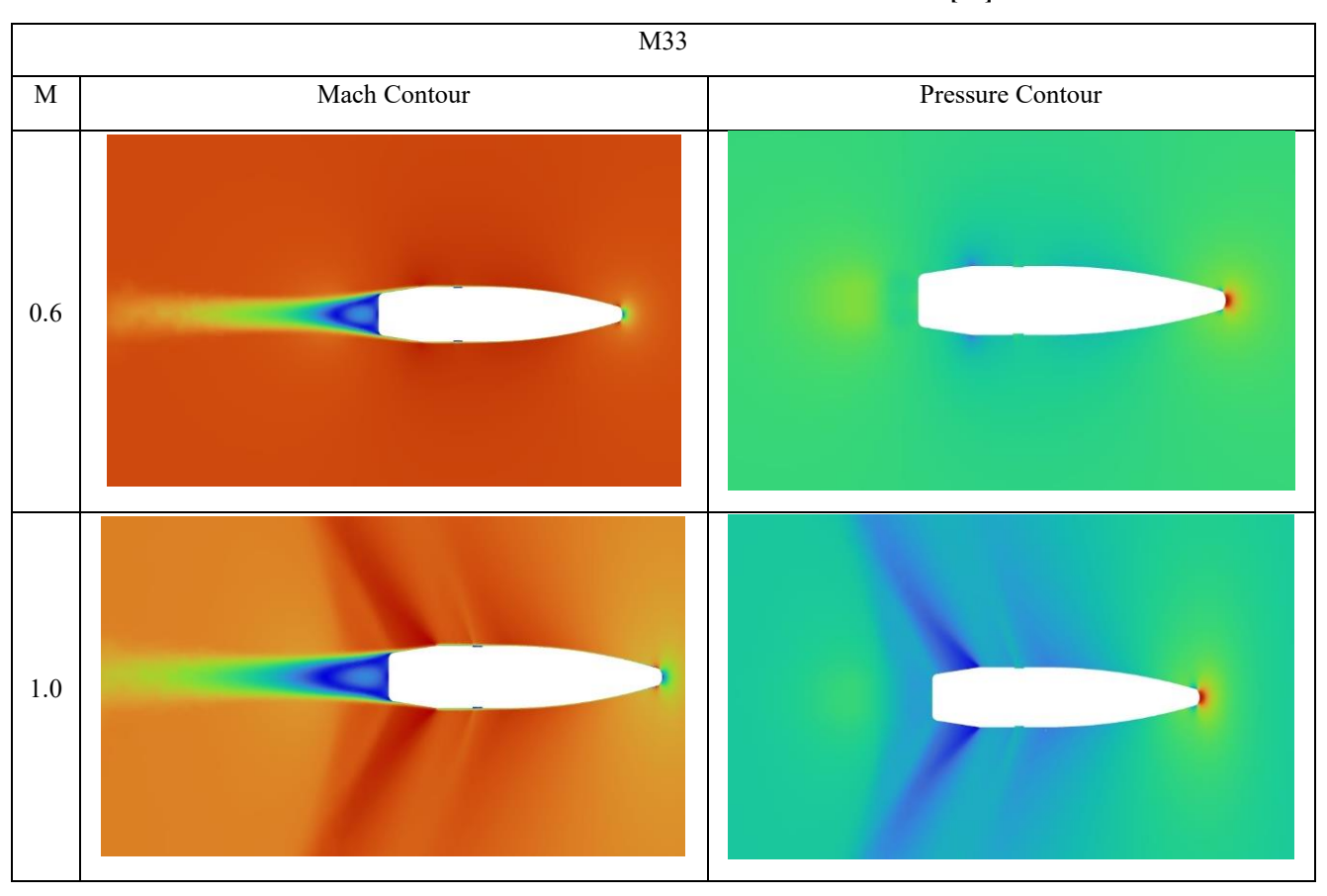
Table 6. Maximum pressure coefficients at projectiles base for zero angle of attck.

Maximum base pressure coefficient									
Mach number	0.6	0.8	0.9	1	1.1	1.2	1.5	2	2.5
M33 9 BT	0.045	0.05	0.058	-0.093	-0.088	-0.097	-0.109	-0.104	-0.093
SBC	0.02	0.028	0.028	-0.107	-0.114	-0.127	-0.126	-0.124	-0.107
LBC	0.018	0.026	0.038	-0.11	-0.115	-0.122	-0.117	-0.104	-0.088

#### 5.1 Flow Field

Tables 7, 8, and 9 show flow field contours. Namely, Mach number and static pressure. Each table represents one configuration at 0.6, 1.0, 1,5, and 2.5 Mach numbers and at zero angle of attack. As can be seen at supersonic speed, a shock wave is formed in front of projectiles. As speed increases the shock wave angle decreases. In addition, the shock wave never attaches the body, because of high nose bluntness. At Mach 1 there is no shock wave created at the nose, though an expansion wave can be noticed at the start of each boattail followed by a shock wave at the base. However, in arc BT the expansion is gradual. Furthermore, unlike other configurations where flow separate at the boattail edge, in arc BT and 7° BT the separation is delayed. Examining riblets BT, a series of shock waves occurs at boattail which explain the high drag at transonic speeds.

Table 7. Pressure and Mach number contours for M33 [21].



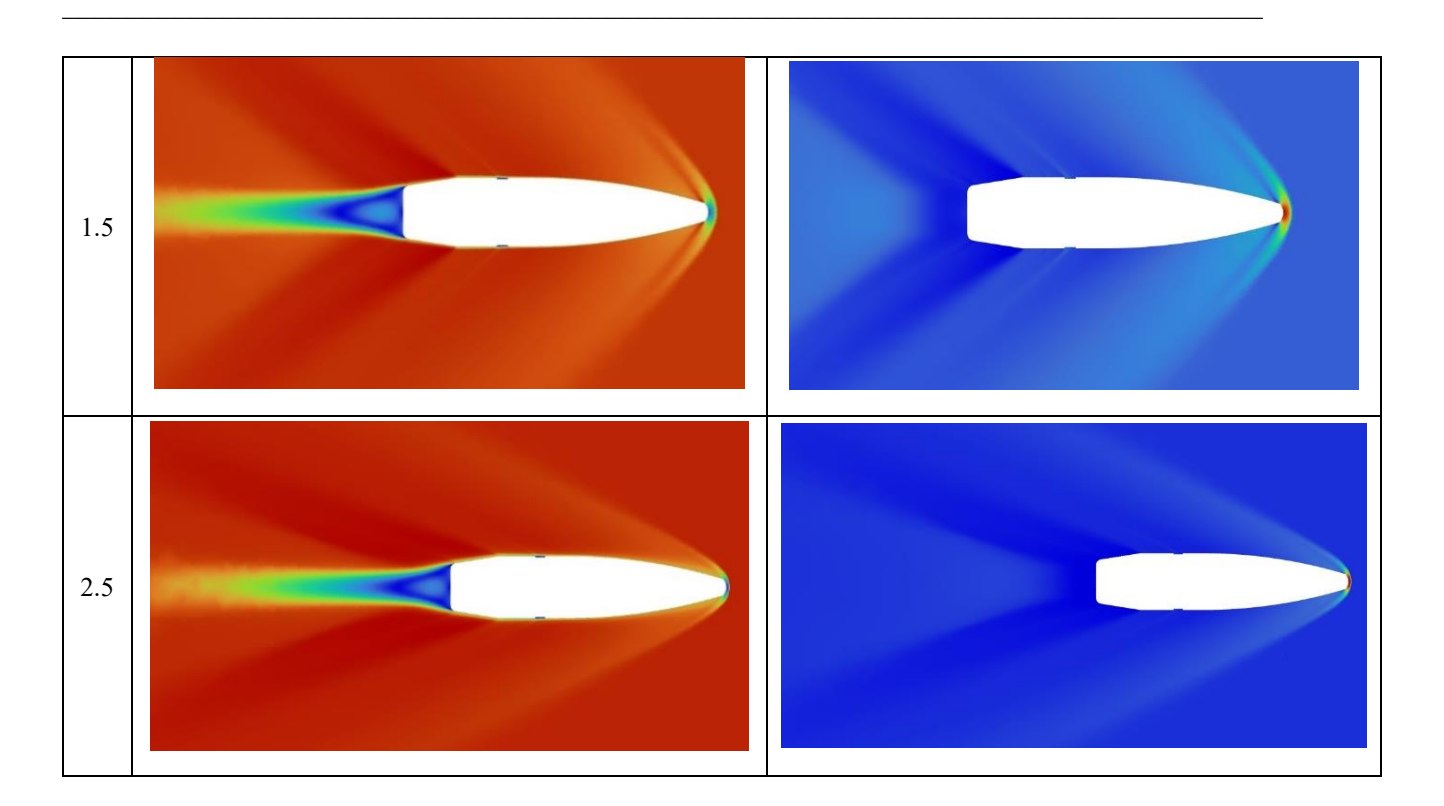
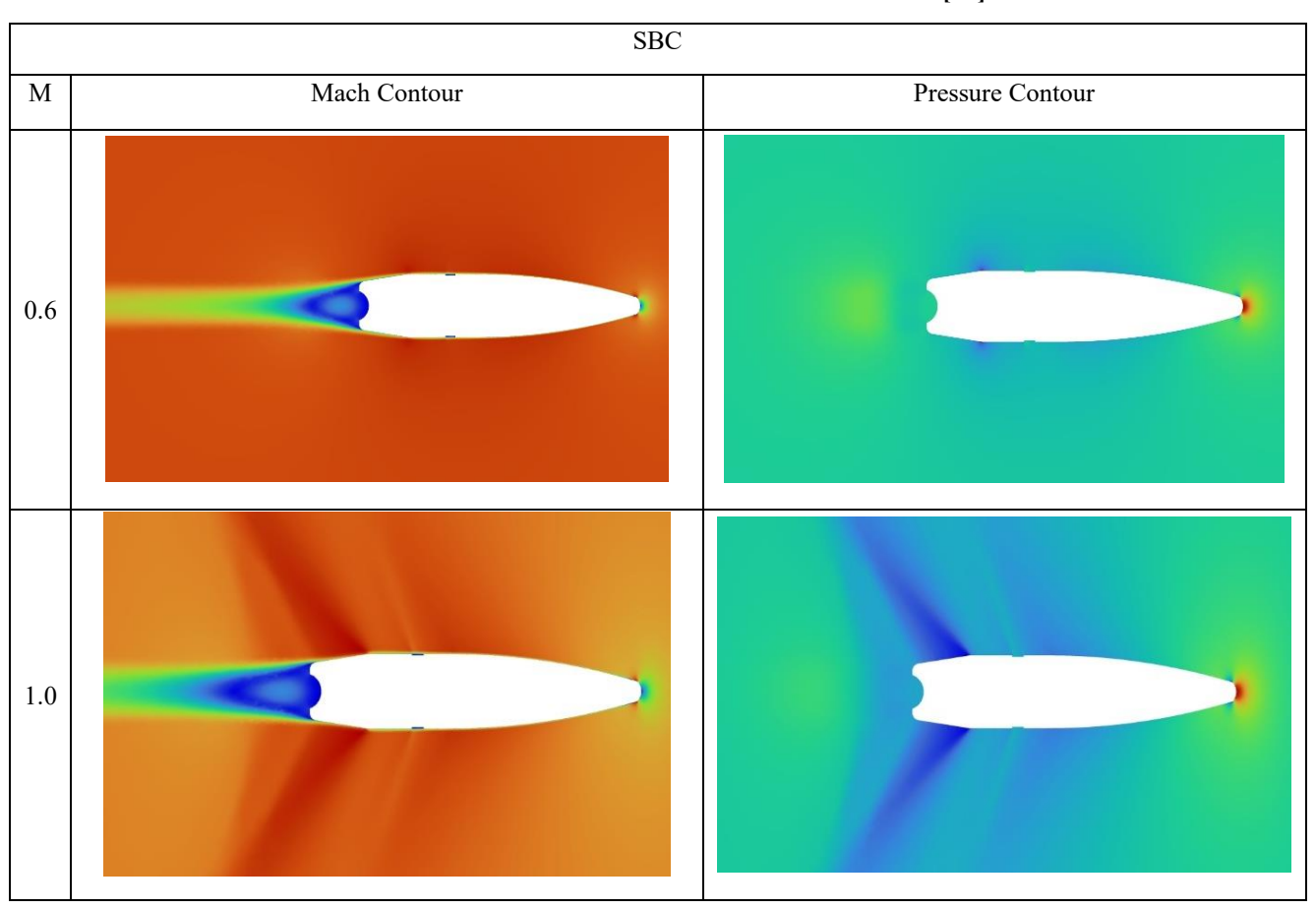


Table 8. Pressure and Mach number contours for SBC [21].



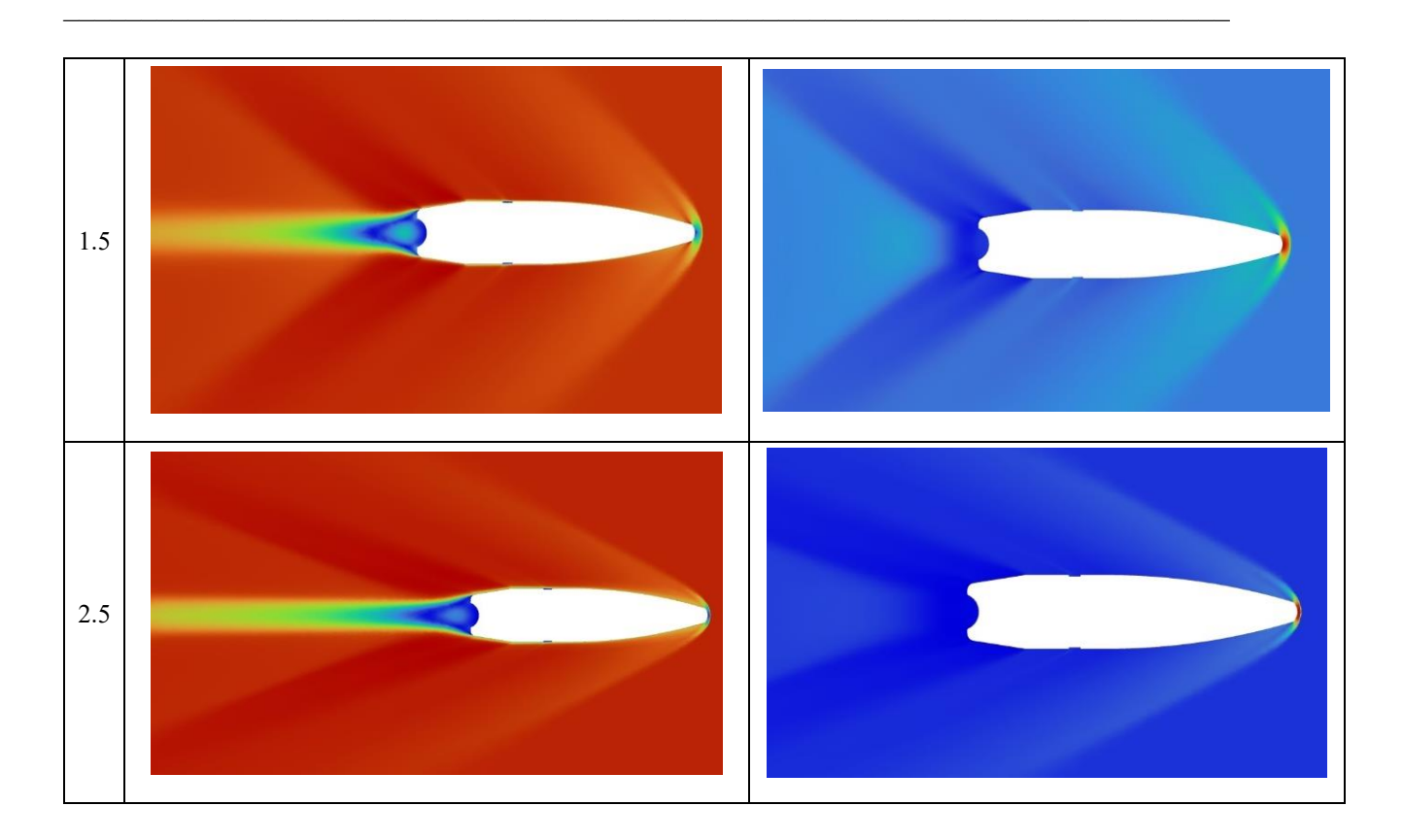
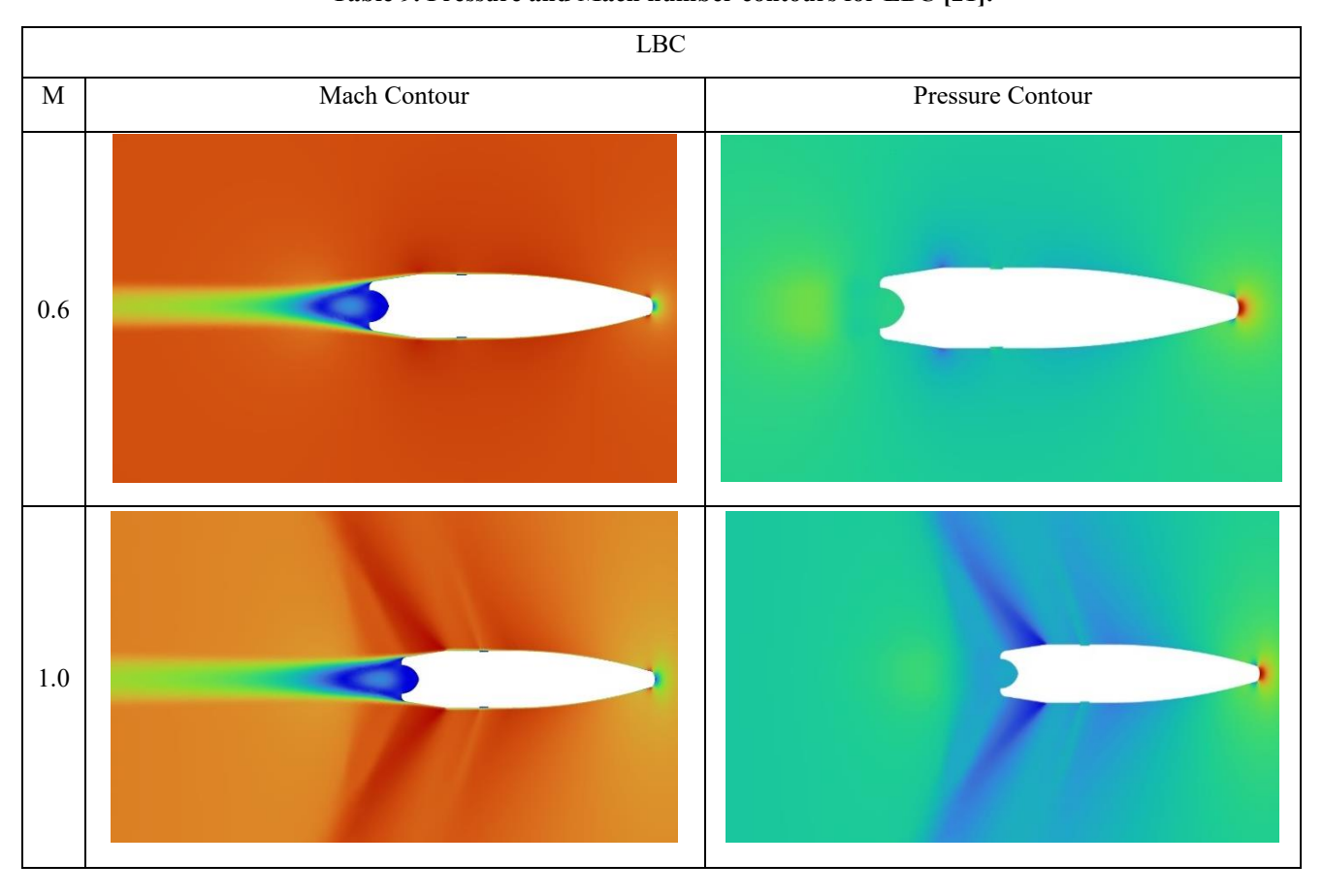
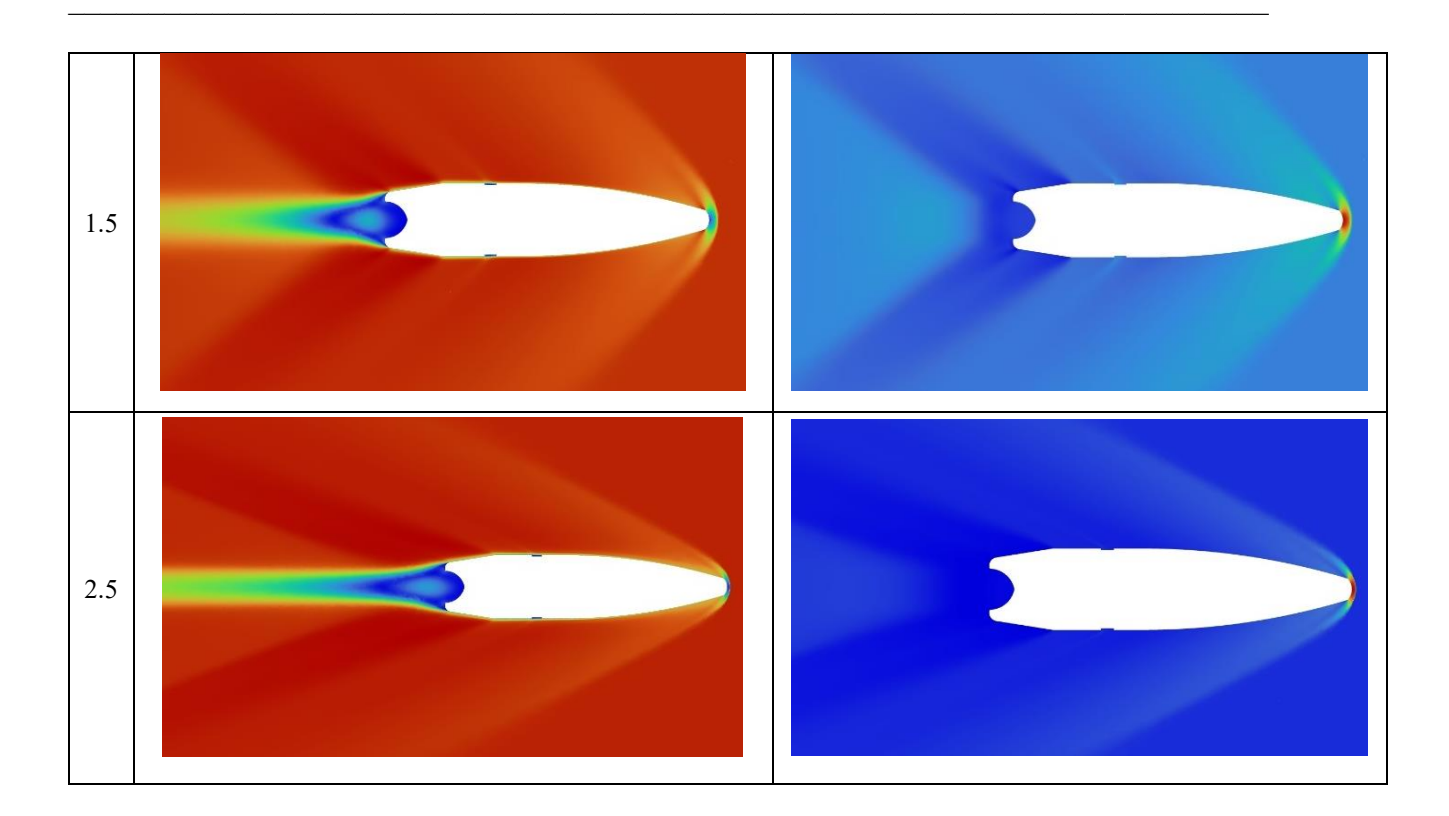


Table 9. Pressure and Mach number contours for LBC [21].





#### 6 Conclusion

This work discusses the aerodynamic characteristics of spinning projectiles, aiming to modify projectiles base to enhance aerodynamic performance. The calculation of main aerodynamic forces and moments are elucidated. They are drag force, lift force, magnus force, magnus moment, overturning moment, and spin damping moment. In the literature, there are many boattailing and range extending technique that are discussed here. Thus, base cavity technique is modified and implemented in this work. The selected projectile for the study is M33 12.95 mm caliber projectile.

The analysis in this work is done by computational fluid dynamics CFD where the flow is three dimensional, compressible, viscous, and involves supersonic speed in some cases. ANSYS fluent is utilized to solve the governing equations. They include continuity equation, three momentum equations, energy equation, ideal gas equation and equation of estate. The speed varies from subsonic to subsonic, where the angle of attack is set to  $0^{\circ}$ ,  $2^{\circ}$  and  $4^{\circ}$ .

Generally, base cavity has minor effect on most of aerodynamics coefficients. Though, large base cavity has low zero-yaw drag relative to the reference projectile. This is due to the reduction in the base drag. In addition, base cavity shows considerably low yaw drag. Because of this reduction in yaw drag as well as the reduction in the linear lift coefficient, it can be said that base cavity could be beneficial at long range firing, as the yaw of repose increases.

## References

- [1] R. McCoy, Modern Exterior Ballistics The Launch and Flight Dynamics of Symmetric Projectile, Atglen: Schiffer Publishing Ltd, 1998.
- [2] "Extirior Ballistic Tables Based on Numerical Integration," U.S Army, 1924.
- [3] E. E. Herrmann, "Range and Ballistic Tables," U.S. Naval Ordnance, 1926.
- [4] W. Blake, "Missile DATCOM User Manual," Air Force Research Laboratory, Ohio, 1998.
- [5] A. T. Associate, "PRODAS Version 3 Technical Manual," Arrow Tech Associate, South Burlington, 2002.

ISSN: 1004-499X Vol. 37 No. 1 (2025)

- [6] F. Moore and T. Hymier, "The 2002 Version of the Aeroprediction code: Part II user's guide," U.S. Naval Surface Warfare Center, Dahlgren Div., 2004.
- [7] S. Silton, "Navier-Stokes Computation for a spinning projectile From Subsonic to Supersonic," *Journal of Spacecraft and Rockets*, vol. 42, no. 2, pp. 223-231, 2005 DOI: 10.2514/1.4175.
- [8] J. Sahu, "Time-Accurate Numerical Prediction of Free Flight," *Journal of Spacecraft and Rockets*, vol. 45, no. 5, 2008.
- [9] A. Ko, K. Chang, D.-J. Sheen, C.-H. Lee, Y. Park and S. W. Park, "Prediction and Analysis of the Aerodynamic Characteristics of a Spinning Projectile Based on Computational Fluid Dynamics," *Hindawi International Journal of Aerospace Engineering*, vol. 2020, pp. 1-12, 2020 DOI: 10.1155/2020/6043721
- [10] W. Calarese, "GAU-8 Projectile afterbody Drag Reduction by Boattailing and Base Injection with Heat Addition," *Journal of Spacecraft and Rockets*, vol. 17, no. 1, pp. 47-52, 1980 DOI: 10.2514/3.57706
- [11] S. Silton and S. Dinavahi, "Base Drag Considrations on a 0.5-Caliber Spinning Projectile," in *26th Applied Aerodynamics Conference*, Hawaii, 2008 DOI: 10.2514/6.2008-6739.
- [12] P. Viswanath, "Drag Reduction of Afterbodies by Controlled Separated Flows," *AIAA Journal*, vol. 39, pp. 73-78, 2001 DOI: 10.2514/3.14699.
- [13] J. DeSpirito, "Effect of Base Shape on Spin-Stabilized Projectiles Aerodynamics," in 26th AIAA Applied Aerodynamics Conference, Hawaii, 2008 DOI: 10.2514/6.2008-6738.
- [14] A. E, A. J, A. R, S. P, K. Sundarraj, P. Kulkarni, M. Veetil and G. P. R, "Computational Study of Aerodynamic Characteristics of a Projectile by Varying Boat Tail Configuration," in *21st Annual CFD Symposium*, Bangalore, 2019 DOI: 10.1007/978-981-16-0698-4 33.
- [15] C. Murphy, "Free Flight Motion of Symmetric Missiles," Ballistic Research Laboratories, 1963 DOI: 10.21236/ad0442757.
- [16] "STANAG 4355 JAIS The Modified Point Mass and Five Degree of Freedom Trajectory Models.," NATO Standardization Agency, 2009.
- [17] R. Cayzac, E. Carette, P. Denis and P. Guillen, "Magnus Effect: Physical Origins and Numerical prediction," *Journal of Applied Mechanics*, vol. 78, September 2011 DOI: 10.1115/1.4004330.
- [18] J. Seifert, "A review of the Magnus effect in aeronautics," *Progress in Aerospace Sciences*, vol. 55, pp. 17-45, 2012 DOI: 10.1016/j.paerosci.2012.07.001.
- [19] D. Carlucci and S. Jacobson, Ballistics Theory and Design of Guns and Ammunition, CRC press, 2007.
- [20] B. Guidos and S. Chung, "Computational Flight Design of .50 Caliber Limited Range Ammunition," in *33rd Aerospace Sciences Meeting and Exhibit*, 1995 DOI: 10.2514/6.1995-63.
- [21] ANSYS, Fluent, ANSYS Inc, 2022R1.
- [22] R. McCoy, "The Aerodynamic Characteristics of 50 Ball, M33, API, M8, and APIT, M20 Ammunition," Ballistic Research Laboratory, Maryland, 1990.
- [23] J. DeSpirito and K. R. Heavey, "CFD Computation of Magnus Moment and Roll Damping Moment of a Spinning Projectile," ARL, 2006.
- [24] ANSYS, Mesh, ANSYS Inc, 2022R1.

#### **Funding**

This Work is Funded by King Fahd University of Petroleum and Mineral